Fluorescence Enhancement of Lignin-based Carbon Quantum Dots by Concentration-dependent and Electron-donating Substituents Synergy and Their Cell Imaging Application

Siyu Zhao [a, b], *Xinrui Chen* [a, b], *Caixia Zhang* [a, b], *Peitao Zhao* [c], *Arthur J. Ragauskas* [d, e, f], *Xueping Song* [a, b] *

[a] College of Light Industry and Food Engineering, Guangxi University, Nanning, 530004, PR China

[b] Guangxi Key Laboratory of Clean Pulp & Papermaking and Pollution Control, Nanning, 530004, PR China

[c] School of Electrical and Power Engineering, China University of Mining and Technology, Xuzhou, 221116, PR China

[d] Department of Chemical and Biomolecular Engineering, University of Tennessee, Knoxville, TN, USA

[e] Joint Institute for Biological Sciences, Biosciences Division, Oak Ridge National Laboratory, Oak Ridge, TN, USA

[f] Center for Renewable Carbon, Department of Forestry, Wildlife and Fisheries, The University of Tennessee, Knoxville, TN 37996, USA

KEYWORDS: Black liquor lignin; Carbon quantum dots; Hydrothermal carbonization; Concentration-dependent; Electron-donating substituent; Fluorescence property

ABSTRACT: Black liquor is an important pollutant in pulp industry, but it also has the potential for high-value utilization. In this study, lignin extracted from black liquor was hydrothermally prepared lignin-based carbon quantum dots (L-CQDs) using a one-pot method. Physicochemical characterization suggested that the L-CQDs exhibited a lamellar core–shell multilayered graphene structure surrounded by oxygen-containing functional groups. The fluorescence intensity of L-CQDs was strengthened depending on their own concentration-dependent and the doping of external groups. The fluorescence intensity of L-CQDs varied between 89.09 and 183.66 under different concentrations, and the most-intense fluorescence (183.66) was obtained at 0.1 $mg \cdot mL^{-1}$. At hydroxyl and amino adsorption capacities of 11.08 and 0.98 $mmol \cdot g^{-1}$, the hydroxylated RL-CQDs-5 and aminated NL-CQDs-3 exhibited the highest fluorescence intensities at 689.22 and 605.39, respectively. Moreover, when pristine L-CQDs were sequentially aminated and hydroxylated, the NRL-CQDs fluorescence intensity reached 1224.92. Cell imaging experiments proved that cells cultivated with NRL-CQDs have brighter fluorescence compared with L-CQDs. The results will render L-CQDs more suitable for practical applications.

INTRODUCTION

Black liquor is one of the main pollutants in the pulp and paper industry [1]. It mainly consists of numerous residual alkali and some organic compounds including hemicellulose, cellulose, and lignocellulose-derived extracts such as lignin [2]. Black liquor exhibits a deep color and a peculiar odor and is highly toxic. If black liquor is discharged directly into natural water, it will severely the environment. Currently, the most common industrial method of treating black liquor in paper mills involves recovering both alkali chemicals and heat energy by burning concentrated black liquor [3]. Although this method is environmentally somewhat benign, it barely recovers any black liquor resources and is wasteful.

Carbon quantum dots (CQDs) are quasi-zero-dimensional fluorescent nanomaterials that were first discovered in 2004 [4]. Since then, they have attracted the attention of scholars worldwide. CQDs offer many advantages such as good water dispersibility [5], excellent biocompatibility [6], and excellent chemical and fluorescence stability [7], and they have been extensively applied to bioimaging [8], metal-ion and drug detection [9], photocatalysis [10], and drug delivery [11]. The current consensus on the CQD structure is that CQDs exhibit the aromatic polymerization of highly ordered graphene combined with rich oxygen-containing functional groups at the edges [12]. Interestingly, owing to its many aromatic rings and hydroxyl, carbonyl, methoxy, and other oxygen-containing functional groups, the structure of lignin is similar to that of CQDs. Therefore, lignin is undeniably a high-quality raw material for preparing CQDs, which also provides a method of utilizing highly valuable black liquor resources. Among the current methods of preparing CQDs, the commonly used hydrothermal carbonization

(HTC) is one of the simplest and most economical and environmentally friendly. However, CQDs hydrothermally prepared by a simple one-pot method usually exhibit poor fluorescence and low quantum yield, which limits their application as fluorescent materials. Therefore, maximizing the fluorescence of CQD is the currently the focus of several investigations.

In most studies, CQD fluorescence has been improved by tuning the inherent CQD properties and doping them with various functional groups. Because the fluorescence of CQDs is typically manifested in the solution state, CQD powder is redissolved in water to prepare a solution containing a certain concentration before its optical properties can be explored, and diverse studies have been reported. For example, Huang et al. [13] used nitrogen-containing *Bauhinia* flowers as a carbon source to hydrothermally synthesize N-CQDs. The N-CQD fluorescence was optimized at 355 nm for an N-CQD concentration of 5.75 $mg \cdot mL^{-1}$. Lv et al. [14] hydrothermally synthesized N-CQDs from citric acid and ethylenediamine (EDA) as the carbon and nitrogen sources, respectively, and found that the optimal N-CQD excitation wavelength was 350 nm for an N-CQD concentration of 0.01 $mg \cdot mL^{-1}$. Li et al. [15] used protein-rich silk as a carbon source to hydrothermally synthesize carbon nanospheres (CNSs) exhibiting quantum yields up to 38%, and the CNS fluorescence was the most intense when the excitation wavelength was 330 nm. Although all these studies have made important contributions to the application and research and development of CQDs, the optimal CQD fluorescence was vastly different in each study because of the lack of experimental standards or optimization of the CQD concentration. Our preliminary work has also demonstrated

that varying the CQD concentration plays an important role in optimizing CQD fluorescence; in other words, CQD fluorescence intensity is strongly concentration dependent. Therefore, it is necessary to explore the fundamental relationship between CQD concentration and fluorescence to maximize the latter prior to doping CQDs.

The introduction of fluorescent functional groups to CQD surfaces can also affect CQD fluorescence. Fluorescent substances typically contain highly conjugated systems such as benzene rings [16]. CQDs contain many π-bond structures in the aromatic rings, which is the main origin of CQD fluorescence. Therefore, enhancing the number and strength of the conjugated structures in CQDs is the key to improving CQD fluorescence. In addition, appropriate substituents must be chosen because they significantly affect conjugated systems [17]. For example, Ju and Chen [18] prepared nitrogen-doped graphene quantum dots (N-GQDs) by pyrolysis wherein citric acid and hydrazine were used as the carbon and nitrogen sources, respectively. Nitrogen doping significantly improved the GQD photoluminescence (PL) emission, and the N-GQD quantum yield significantly increased to 23.3%. The highly efficient N-GQD PL emission was reported to originate from the N-doping-induced modulation of the chemical and electronic characteristics of the GQDs. X-ray photoelectron spectroscopy (XPS) results showed that the N dopants primarily comprised amino N atoms, indicating that the enhanced N-GQD fluorescence may be attributed to the amino-group- and benzene-ring-generated structure. Shen et al. [19] prepared CDs from lampblack and HNO_3 by chemical oxidation. The obtained CQD solution was then treated with sodium borohydride at room temperature for 2 d to reduce the C=O groups

in the CQDs to -OH. The CQD quantum yield increased from 1.55 to 7.25%, further confirming the influence of the -OH content of CQDs on its fluorescence. These examples illustrate that the nitrogen-doped amino and reduction-generated hydroxyl groups, both electron-donating substituents, could combine with CQD benzene rings to form aniline and phenol structures, thus generating p–π conjugation and intensifying CQD fluorescence. However, most studies to date have mainly focused on modifying a single functional group rather than exploring the interactions of different substituents. Hence, the synergistic or antagonistic effects of different electron-donating substituents on CQD fluorescence should be studied to improve CQD fluorescence.

Therefore, in this study, alkali lignin was extracted from black liquor and was used as a carbon source to hydrothermally prepare lignin-based CQDs (L-CQDs) by a simple one-pot method. Then, the pristine-L-CQD fluorescence potential was fully explored to elucidate the L-CQD-concentration-dependent, and electron-donating groups such as -NH_2 and -OH were introduced to the L-CQD surfaces to maximize the doped-L-CQD fluorescence. Additionally, the synergistic influence of -NH_2 and -OH on L-CQD fluorescence was explored. After that, L-CQDs were applied to cell imaging to prove the value of fluorescence enhanced modification. The study findings will provide guidance for improving the fluorescence of hydrothermally prepared biomass-based CQDs and make it more suitable for practical applications.

EXPERIMENTAL SECTION

Materials

Bagasse-derived caustic-soda black liquor (16.73 wt.% solids; pH 10.54) was

obtained from Guangxi Guitang Co., Ltd., China. Sulfuric acid (98%), sodium hydroxide, anhydrous ethanol, sodium borohydride, ammonia, urea, EDA, ethylenediaminetetraacetic acid (EDTA), and quinine sulfate were purchased from Aladdin Reagent Co., Ltd. (Shanghai). All the chemicals were of analytical grade and were used as purchased. Ultrapure water was prepared using a Milli-Q® ultrapure water purification system (Merck KGaA, Germany). HepG2 cells were purchased from iCell Bioscience Co., Ltd. (Shanghai). Fetal bovine serum (FBS), dulbecco's modified eagle medium (DMEM), and phosphate buffer (PBS) were purchased from Biological Industries (Israel).

Preparation of alkali lignin

Alkali lignin was extracted from the black liquor by acid precipitation. First, the black liquor was heated at 3 °C /min to 55 °C, at which it was maintained for 30 min. Meanwhile, 30 wt.% sulfuric acid was added dropwise to the black liquor to adjust the pH to 3, which precipitated a flocculent from the black liquor. The temperature was maintained at 55 °C for another 30 min to completely precipitate the flocculent. The suspension was centrifuged, and the flocculent precipitate was dialyzed [molecular weight cutoff (MWCO) =1000 Da] to remove excess sulfuric acid and small molecules until the dialysate pH was 7. Then, 3 volumes of anhydrous ethanol were added to the dialyzed precipitate, which was left to settle for 4 h to further purify the lignin. Finally, the suspension was vacuum-filtered, and the obtained solid was vacuum-dried at 60 °C for 24 h and then ground using an agate mortar to obtain the alkali lignin.

Preparation of lignin-based carbon quantum dots (L-CQDs)

The alkali lignin was hydrothermally carbonized to prepare the L-CQDs. First, 1 g of the alkali lignin and 30 mL of ultrapure water were added to a 50-mL polytetrafluoroethylene (PTFE)-lined stainless-steel reactor and ultrasonicated for 10 min to uniformly mix the reactants. The reactor was then oven-heated at 5 °C/min to 180 °C, where it was maintained for 12 h. After the reaction, the reactor was naturally cooled to room temperature. Then, the products were centrifuged at 10000 rpm for 20 min to separate the supernatant from the solids. The supernatant was then dialyzed in ultrapure water for 5 d with a 3500-Da-MWCO dialysis bag, and the ultrapure water was replenished every 6 h. The obtained dialyzed liquid was rotary-evaporated at 60 °C to remove the excess water. The concentrated solution was freeze-dried to obtain the L-CQD powder.

L-CQD-concentration optimization

The L-CQD powder was dissolved in ultrapure water to prepare a mother liquor (1 $mg \cdot mL^{-1}$ L-CQD solution), which was further diluted to prepare solutions containing 0.5, 0.2, 0.1, 0.05, or 0.02 $mg \cdot mL^{-1}$ of L-CQDs (denoted as L-CQDs-X, where X was in the range 1–5 and corresponded to the above concentration of L-CQDs, respectively). The optimal excitation and emission wavelengths and fluorescence intensity of the L-CQDs-1–5 solutions were measured using a fluorescence spectrophotometer (RF-5301PC, Hitachi, Japan).

Introduction of electron-donating substituents to L-CQD surfaces

The electron-donating substituents (i.e., hydroxyl and amino groups) were introduced to the surfaces of the hydrothermally prepared L-CQDs by reduction with

$NaBH_4$ and an aminating reagent, respectively.

Introduction of hydroxyl groups

L-CQD samples in which the concentration was optimized to exhibit the highest intensity L-CQD fluorescence according to the method described in Section "**L-CQD-concentration optimization**" were used for further experiments. Different concentrations of the reducing agent ($NaBH_4$) were added to the samples such that the L-CQD/$NaBH_4$ mass ratios were 1:0.2, 1:0.5, 1:1, 1:1.5, 1:2, or 1:3. All the samples were magnetically stirred for 2 h at room temperature to prepare six samples of reduced-lignin carbon quantum dots (denoted as RL-CQDs-X, where X was in the range 1–6 and corresponded to the above mass ratios of L-CQDs/$NaBH_4$, respectively). The optimal excitation and emission wavelengths and fluorescence intensity of the hydroxyl-modified L-CQD samples were measured using a fluorescence spectrophotometer (Hitachi RF-5301PC, Japan). The RL-CQD sample exhibiting the most intense fluorescence was dialyzed (500 Da) to remove the excess $NaBH_4$, rotary-evaporated, and freeze-dried according to the method described in Section "**L-CQD-concentration optimization**" to obtain the RL-CQD powder used for further testing.

Introduction of amino groups

The amino groups were introduced to the L-CQD surfaces using the same method described in Section "**Introduction of hydroxyl groups**". The L-CQDs sample with the highest fluorescence intensity based on the optimization concentration in Section "**L-CQD-concentration optimization**" was used in the subsequent experiments. Amination reagents (i.e., ammonia, urea, EDA, or EDTA) were added to the L-CQD

samples such that the L-CQD/amination reagent mass ratio was 1:1 to prepare solutions containing aminated-lignin carbon quantum dots (NL-CQDs-X). Then, 30 mL of the solution was added to a 50-mL PTFE-lined stainless-steel reactor and heated at 180 °C for 3 h. After the reaction, the reactor was repeatedly washed with ice water until it cooled to room temperature. The solution was collected from the reactor to obtain samples modified by different amination reagents (denoted as NL-CQDs-X, where X was in the range 1–4). The NL-CQDs-1–4 corresponded to the ammonia, urea, EDA, and EDTA amination reagents, respectively. The optimal excitation and emission wavelengths and fluorescence intensity of the aminated samples were determined using a fluorescence spectrophotometer (Hitachi RF-5301PC, Japan). The NL-CQDs-3 sample exhibiting the most intense fluorescence was dialyzed (500 Da) to remove the excess amination reagent, rotary-evaporated, and freeze-dried according to the method described in Section "**L-CQD-concentration optimization**" to obtain the NL-CQDs-3 powder used for further testing.

Co-introduction of amino and hydroxyl groups

Both modification methods were sequentially used to prepare L-CQDs exhibiting high-intensity fluorescence. Briefly, L-CQDs (optimal concentration = 0.1 $mg \cdot mL^{-1}$) were hydrothermally treated with the amination reagent (EDA), and the L-CQDs/EDA mass ratio was 1:1. Then, the aminated L-CQDs was further hydroxylated with the reducing reagent ($NaBH_4$), and the mass ratio of aminated L-CQDs and $NaBH_4$ was 1:2. The amine and hydroxyl co-modified CQDs (NRL-CQDs) were prepared following the same methods as described in Sections "**Introduction of hydroxyl**

groups" and "**Introduction of amino groups**", respectively, and their fluorescence was measured according to the method described in Section "**L-CQD-concentration optimization**".

The entire experimental procedure of this word was shown in Scheme S1.

Quantum yield

The CQD quantum yields (QYs) were calculated using quinine sulfate (dissolved in 0.05 mol/L sulfuric acid; QY = 0.54) as a reference. At the optimal excitation wavelength of each sample, the CQD QY was calculated using the following formula [20]:

$$QY = QY_{qs} \cdot \frac{S}{S_{qs}} \cdot \frac{A_{qs}}{A} \cdot \frac{\eta^2}{\eta^2_{qs}}, \quad (1)$$

where *QY* is the quantum yield, *qs* represents the quinine-sulfate reference solution, *S* means the integral area of the fluorescence peak in the PL spectra, *A* expresses the absorbance at the excitation wavelength, and η represents the refractive index of the solution.

L-CQD characterization

A Fourier-transform infrared (FT-IR; Bruker TENSOR II, Germany) spectrometer operating in attenuated total reflectance (ATR) mode was used to elucidate the L-CQD chemical structure. X-ray photoelectron spectroscopy (XPS, Thermo Fisher Scientific^{TM} K-alpha^{+}, USA) was used to measure the carbon, oxygen, and nitrogen contents and the functional-group compositions on the pristine- and modified-L-CQD surfaces. The full-scan XPS spectra were scanned first and then the narrow-scan C 1*s*, O 1*s*, and N 1*s* spectra were scanned. The pristine- and modified-L-CQD

microstructures were observed by transmission electron microscopy (TEM, FEI TECNAI G2 F30, USA) operating at 300-kV acceleration. Atomic force microscopy (AFM, Hitachi 5100N, Japan) was used to observe the 2- and 3-dimensional L-CQD structures and mica sheets were used as the carrier. The pristine- and modified-L-CQD fluoroluminescences (FLs) were measured using a fluorescence spectrophotometer (Hitachi RF-5301PC, Japan). During the FL measurements, the slit widths of the excitation and emission lights were both 5 nm, and the ordinal-valued PL spectra were used to quantify the fluorescence intensity. An ultraviolet–visible-light (UV–vis) spectrophotometer (Hitachi u-4100 UV–vis, Japan) was used to measure the UV–vis absorption spectra of the pristine and modified L-CQDs.

L-CQD Cytotoxicity assays

The CCK-8 method was used to evaluate the cytotoxicity of L-CQDs and NRL-CQDs to HepG2 cells [21]. The HepG2 Cells were firstly cultured in DMEM medium containing 10% FBS and 1% penicillin/streptomycin. Then, the HepG2 cells at logarithmic growth stage were taken and inoculated into 96-well plates at the rate of 8×10^3 cells per well after cell concentration was adjusted. The cells were incubated overnight in a 37 ℃ constant temperature incubator with 5% CO_2 atmosphere. Then both L-CQDs and NRL-CQDs solutions (0.1 $mg\cdot mL^{-1}$) were dropped into the cells, respectively, and the cells were cultured in a 37 ℃ constant temperature incubator containing 5% CO_2 for 24 h. After that, the medium was removed and each well was washed three times with PBS, and the medium containing 10% CCK-8 was added at the rate of 100 μL/ well. The medium was cultured in the incubator for another 2 h. The

absorbance of the medium at 450 nm was measured with a microplate reader (Tecan SPARK 10M, Switzerland). The cell viabilities values were calculated according to the following formula (A represents absorbance):

$$\text{Cell viability (\%)} = \frac{A_{\text{experimental group}}}{A_{\text{control group}}} \times 100\%, \quad (2)$$

L-CQD cell imaging

The cell imaging abilities of L-CQDs and NRL-CQDs were tested by fluorescence microscopy. HepG2 cells at logarithmic growth stage were inoculated into 96-well plates at the rate of 8×10^3 cells per well. Then, L-CQDs and NRL-CQDs solutions (0.1 $mg\cdot mL^{-1}$) were respectively dropped into the cells, and the cells were cultured in a 37 ℃ constant temperature incubator containing 5% CO_2 for 24 h. After that, the medium was removed and each well was washed three times with PBS. A fluorescence microscope (Olympus IX53, Japan) was used to observe the cultivated cells and capture the fluorescence image (λ=395 nm).

RESULTS AND DISCUSSION

L-CQD-concentration-dependent optical properties

Although CQD fluorescence intensity is traditionally believed to be positively correlated with CQD concentration (that is, the higher the CQD concentration, the more intense the CQD fluorescence), recent reports on CQD-concentration-dependent fluorescence intensity have overturned this view [22]. Specifically, it has been shown that CQDs exhibit the most intense fluorescence at a certain CQD concentration because CQDs exhibit multiple emission sites [23], aggregation-caused quenching (ACQ)/aggregation-induced emission (AIE) [22], particle spacing [24] and

localized/intrinsic states [25]. For example, Shao et al. [23] prepared self-quenching-resistant solid-state fluorescent carbon dots (SSFPCD) with methyl acrylate and ethylamine. Changes in SSFPCD concentration caused SSFPCD to produce blue, green, and yellow emission centers corresponding to the emission centers in states I, II, and III, respectively. State I was derived from the subfluorophore on the CQD surface, and states II and III were generated by the dense polymer-network-protected subfluorophore. Zhang et al. [22] believed CQDs exhibited concentration-dependent fluorescence owing to ACQ/AIE. They found that in solution, with increasing concentration ACQ inhibited the blue CQD fluorescence, while simultaneously, AIE promoted the yellow fluorescence which gradually increased. Moreover, monodisperse CQDs aggregated into polymers exhibiting blue emission with increasing CQD concentration. Wang et al. [24] showed that particle-size spacing might cause CQD-concentration-dependent fluorescence possibly because increasing the CQD particle spacing reduced particle interactions at low CQD concentrations, which blueshifted the PL and increased its intensity with increasing irradiation-light intensity. At high CQD concentrations, the distance between CQD particles decreased and their interaction increased, resulting in the red shift and the decrease of photoluminescence intensity due to self-absorption. Ba et al. [25] reported that CQD-concentration-dependent PL was caused by the localized/intrinsic CQD state because the CQD solution self-assembled at high concentrations, thereby changing the main PL emission center from the intrinsic-state π–π interaction to the localized state owing to electron redistribution and the distortion of oxygen-related functional groups. The gap between the excited and

ground states of the dominant localized state might be narrower than that between the excited and intrinsic states, which would broaden and red-shift the photon-radiation absorption band. Typically, the optical properties (e.g., fluorescence intensity, excitation and emission wavelengths, QY, and fluorescence color) of CQD solutions with varying CQD concentrations differ considerably. Therefore, optimizing the CQD concentration is an effective method of improving the PL of pristine CQDs.

L-CQD solutions prepared using 0.5, 0.2, 0.1, 0.05, or 0.02 $mg \cdot mL^{-1}$ of L-CQDs (denoted as L-CQDs-1–5, respectively), were used in the experiment. The emission spectra were generated at the optimal excitation wavelength for each sample, and the results are shown in Figure 1 (a). With decreasing L-CQD concentration, the optimal excitation and corresponding emission wavelengths both gradually blueshifted, and the fluorescence first intensified and then weakened, which is consistent with the findings of Shao et al. [23]. The fluorescence intensity of each sample varied between 89.09 and 183.66, and the L-CQDs-3 exhibited the most intense fluorescence at a concentration of 0.1 $mg \cdot mL^{-1}$. Therefore, 0.1 $mg \cdot mL^{-1}$ was selected as the optimal L-CQD concentration for the next experiment. The optimization of LC-CDs concentration maximizes its own fluorescence intensity.

Figure 1 (b) shows the PL spectra generated for L-CQDs-3. As the excitation wavelength was increased from 330 to 420 nm, the L-CQDs-3 fluorescence first intensified and then weakened. At an excitation wavelength of 370 nm, L-CQDs-3 emitted the most intense fluorescence, and the corresponding emission wavelength was 461 nm. In addition, unlike the emission wavelength of inorganic quantum dots [26], that

of L-CQDs-3 redshifted with increasing excitation wavelength, thereby exhibiting excitation-wavelength dependence This result may be due to the solvent relaxation of polar groups of the CQD graphene-oxide structure in polar solvents such as water, which is known as the "giant red-edge effect" [26]. Moreover, L-CQDs-3 exhibited excellent fluorescence stability: only 5% of the fluorescence intensity was lost after the sample was stored at room temperature for three months.

As shown in Figure 1 (c), L-CQDs also exhibit up-conversion emission, which implies that L-CQDs can be excited by long-wavelength, low-frequency light and emit short-wavelength, high-frequency light (anti-Stokes) [27] in contrast to traditional PL. This behavior enables L-CQDs to effectively convert near-infrared light to visible light. As shown in Figure 1 (c), L-CQDs-3 irradiated/excited by near-infrared light in the range 780–900 nm emitted visible light in the range 478–524 nm, indicating that L-CQDs-3 exhibited excitation-wavelength-dependent fluorescence. However, the fluorescence was weaker than that of conventional PL, and no peaks appeared in the near-infrared band. The L-CQDs-3 electronic transition was measured using UV–vis spectroscopy, and the results are shown in Figure 1 (d). The L-CQDs-3 exhibited a wide absorption band and two weak absorption peaks in the range 200–600 nm. A weak absorption peak appeared near 280 nm, indicating that L-CQDs-3 exhibited a π–π* transition, which might be related to the C=C bonds in the aromatic ring [12]. The appearance of another weak absorption peak near 330 nm indicated that L-CQDs-3 exhibited an n–π* transition, which might be related to the C=O bonds of carbonyl, carboxyl, and aldehyde groups [28]. The insets in Figure 1 (d) show optical photographs

of L-CQDs-3 irradiated under natural sunlight and 365 nm UV light. As show L-CQDs-3 were pale yellow under sunlight excitation and emitted blue light under UV-light excitation.

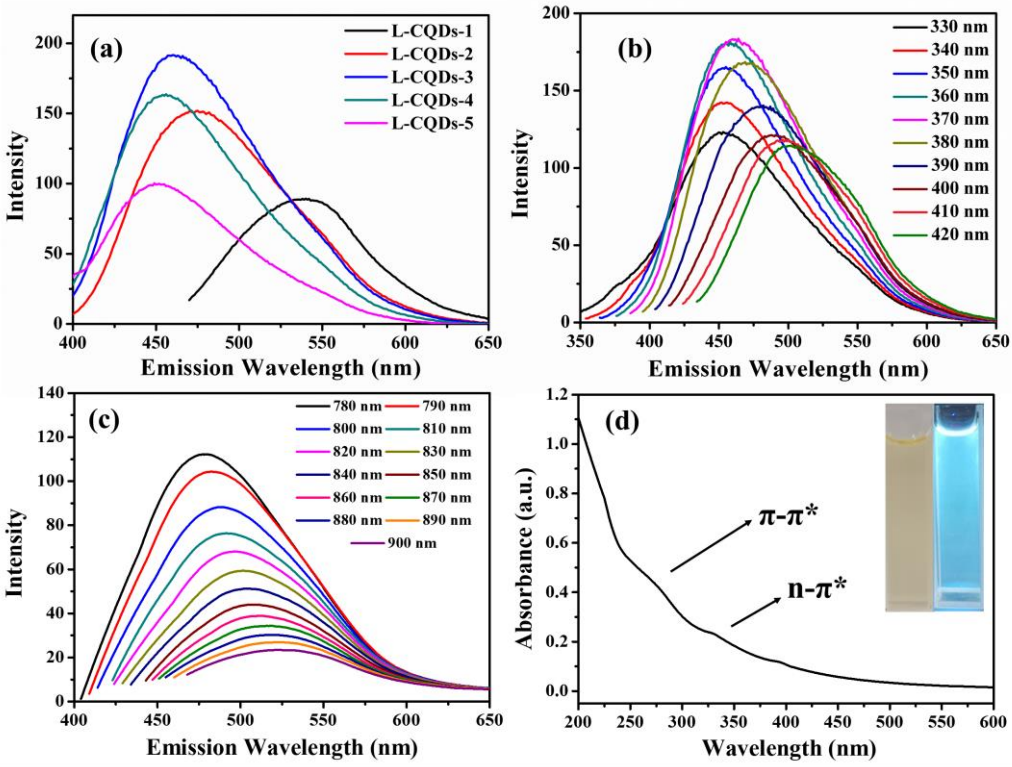

Figure 1. (a) L-CQD-concentration-dependent PL spectra (the concentration of L-CQDs was from 0.02 mg·L^{-1} to 0.5 mg·L^{-1}), (b) L-CQDs-3 PL spectra with the excitation wavelength from 330 nm to 420 nm, (c) L-CQDs-3 up-conversion PL spectra with the excitation wavelength from 780 nm to 900 nm, and (d) L-CQDs-3 UV–vis absorption spectra and optical photographs (inset).

Effects of electron-donating substituents on L-CQD PL

The weak L-CQD fluorescence compared with those of other fluorescent agents, limited its further application, which is also a key disadvantage of other hydrothermally prepared biomass-based CQDs [12, 29]. Therefore, intensifying the L-CQD fluorescence

is the key to rendering L-CQDs suitable for practical applications. Current research suggests that almost all the molecules that can fluoresce contain conjugated double-bond systems [16] and that the larger the conjugated system, the easier the excitation of the delocalized π electrons and the easier the molecule fluoresces. Thus, fluorescent substances, including CQDs, usually contain numerous aromatic or heterocyclic rings. Therefore, increasing the size of the conjugated-double-bond systems is a feasible method of intensifying CQD fluorescence. Substituents strongly influence the fluorescence conversion efficiency of aromatic compounds [17]. Therefore, the excited state of fluorescent substances containing electron-donating substituents such as -NH_2, -NHR, -NR_2, -OH, -OR, or -CN, is usually generated by exciting *n* electrons in the electron-donor group outside the ring which are then transferred to the ring [17]. Because the *n*-electron electron cloud is oriented almost parallel to the aromatic-ring π orbital, the electron-donor group and aromatic ring share the conjugated π-electron structure, thus expanding their mutual conjugated-double-bond system. In addition, the introduction of electron-donating substituents resulted in the formation of p–π electron-donating conjugation with the benzene ring, which further enhanced the degree of π-electron conjugation. Therefore, electron-donating substituents can be introduced to L-CQDs as an important method of enhancing L-CQD fluorescence efficiency. Thus, electron-donating substituents (i.e., hydroxyl and amino groups) were introduced to the L-CQD surface to intensify the L-CQD fluorescence emission through external modification.

L-CQD optical properties

Sodium borohydride ($NaBH_4$) is a very common strong reducing agent, and its main reducing capacity is reflected in its monovalent hydrogen atoms. $NaBH_4$ was used as a reducing agent to modify the L-CQD surfaces, and the results are shown in Figure 2 and Table 1. As shown in Figure 2 (a) and Table 1, with increasing $NaBH_4$ concentration, the fluorescence of the reduced L-CQDs intensified from 183.44 to 693.27, representing an overall intensification of approximately 278%. The QY also increased from 1.65 to 5.90%. Meanwhile, compared with the optimal excitation wavelength for L-CQDs-3, that of the RL-CQDs-X did not change (remaining at 370 nm) upon $NaBH_4$ reduction. As shown in Figure 2 (b) and Table 1, when the L-CQD/$NaBH_4$ mass ratio increased from 1:2 to 1:3, the RL-CQDs-X fluorescence intensity and QY both became saturated and did not increase further. Thus, at an L-CQD/$NaBH_4$ mass ratio of 1:2, RL-CQDs-5 exhibited the most intense fluorescence among all the samples and was therefore selected for subsequent characterization experiments.

Figure 2 (c) shows the RL-CQDs-5 PL spectra, which are similar to those of the L-CQDs and indicate excitation-wavelength-dependent fluorescence. At an excitation wavelength of 370 nm, the RL-CQDs-5 fluorescence had the highest intensity, and the corresponding emission wavelength was 458 nm, similar to that of the L-CQDs (461 nm). Notably, in addition to the first peak at 370 nm in the RL-CQDs-5 PL spectra, the fluorescence first intensified and then weakened between 360 and 440 nm. Thus, a second peak or buffer appeared at 420 nm, which may be caused by the transformation of the L-CQD-surface C=O or -CHO functional groups into -OH by the $NaBH_4$

reducing agent, which changed the multiple emission centers of the L-CQD nuclear, edge, and surface state [30] features which also appear in the other RL-CQDs-X spectra (Figures. S1 (a) and (b) in the Supporting Information).

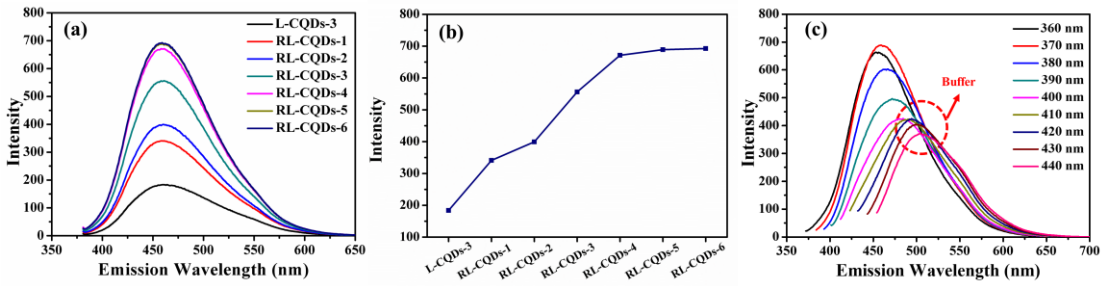

Figure 2. (a) PL spectra generated for L-CQDs reduced using different $NaBH_4$ concentrations and excited using 370 nm light; (b) fluorescence intensity plotted as a function of $NaBH_4$ concentration for L-CQDs excited using 370-nm light; (c) PL spectra generated for RL-CQDs-5 excited using 360–440 nm light.

Table 1. RL-CQDs-X optical properties.

Sample	Optimal excitation wavelength (nm)	Optimal emission wavelength (nm)	Fluorescence intensity	Quantum yield (%)
L-CQDs-3	370	464	183.66	1.65
RL-CQDs-1	370	459	340.93	3.01
RL-CQDs-2	370	460	399.41	3.48
RL-CQDs-3	370	461	556.18	4.78
RL-CQDs-4	370	461	671.44	5.73
RL-CQDs-5	370	459	689.22	5.87
RL-CQDs-6	370	459	693.27	5.90

Amination reagents ammonia, urea, EDA, and EDTA were used as nitrogen sources to introduce amino groups to the surfaces of the hydrothermally prepared L-CQDs. Samples of the different aminated L-CQDs were obtained, and the results are shown in Figure 3. Compared with the L-CQDs-3 fluorescence intensity (Figure 3 (a)), that of the aminated-L-CQDs increased and maintained good excitation-wavelength-

dependent fluorescence. Figures. 3 (b-e) are PL spectra of the aminated L-CQDs and the optimal excitation wavelengths of the aminated L-CQDs are listed in Table 2. The PL spectra generated for the aminated L-CQDs excited at the optimal wavelength are shown in Figure 3 (f). As shown in Figure 3 (f) and Table 2, NL-CQDs-3 exhibited the most intense fluorescence (605.39) among the aminated L-CQDs, representing an increase of approximately 228% compared with the L-CQDs-3 fluorescence. The NL-CQDs-3 QY also increased from 1.65 to 5.54%, which was higher than those of the other aminating reagents. Therefore, the NL-CQD-3 sample was used as the optimal sample for further characterization.

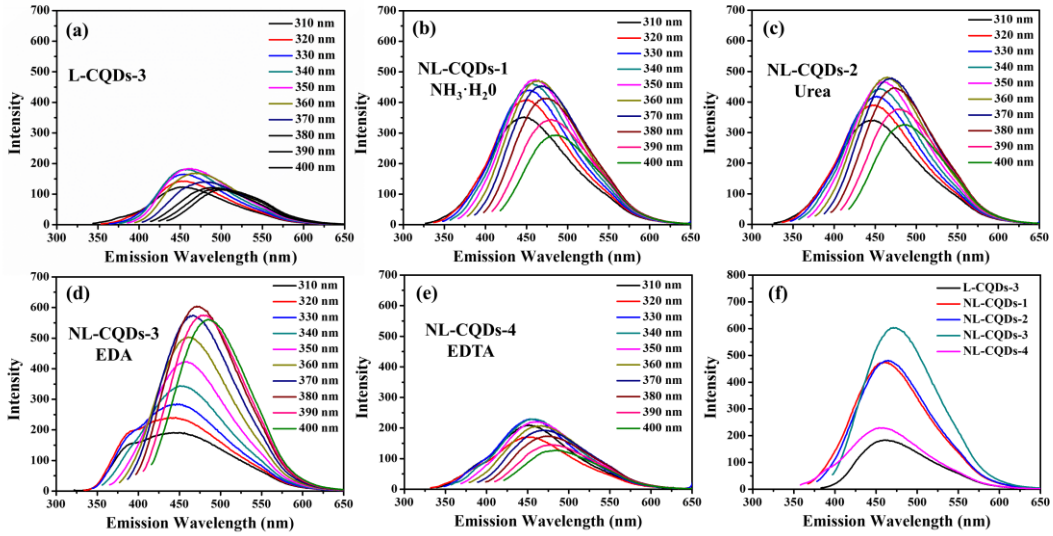

Figure 3. PL spectra generated for (a) L-CQDs-3, (b) NL-CQDs-1 ($NH_3 \cdot H_2O$), (c) NL-CQDs-2 (Urea), (d) NL-CQDs-3 (EDA) and (e) NL-CQDs-4 (EDTA), respectively, excited using 310–400 nm light, and (f) PL spectra generated for NL-CQDs-X excited at each optimal wavelength.

Table 2. NL-CQDs-X optical properties.

Sample	Optimal excitation	Optimal emission	Fluorescence	Quantum

	wavelength (nm)	wavelength (nm)	intensity	yield (%)
L-CQDs-3	370	464	183.66	1.65
NL-CQDs-1	350	458	475.73	4.54
NL-CQDs-2	360	463	485.33	4.50
NL-CQDs-3	380	471	605.39	5.54
NL-CQDs-4	330	457	229.9	2.30

Figure S2 (a) compares the UV–vis spectra generated for the original L-CQDs and both modified L-CQDs. All the CQDs exhibited a broad absorption band in the range 200–600 nm, and weak absorption peaks corresponding to π–π^* and n–π^* transitions appeared at 280 and 330 nm, respectively, indicating that introducing both electron-donating substituents did not change the L-CQD structural framework. Furthermore, the L-CQD bandgap spectra were deduced from the UV–vis ones, as shown in Figure S2 (b). Compared with the original L-CQD bandgap, the RL-CQDs-5 and NL-CQDs-3 ones had widened, further reflecting the hydroxylated and aminated CQDs and explaining the enhanced L-CQD fluorescence QYs [22].

Amine and hydroxyl co-modified NRL-CQDs were then prepared by combining both optimal modification methods, and the corresponding PL spectra are shown in Figure 4 (a). The optimal NRL-CQD excitation wavelength was consistent with those of both L-CQDs-3 and RL-CQDs-5 (370 nm). The NRL-CQD fluorescence intensified, reaching 1224.92 (570% increase compared to the L-CQD-3 fluorescence), indicating that amination and hydroxylation had synergistically intensified the L-CQDs-3 fluorescence. Figure 4 (b) shows the PL spectra generated for an NRL-CQD sample prepared by the simple mixing of RL-CQDs-5 and NL-CQDs-3 in a 1:1 volumetric ratio. The CQD fluorescence was weaker than the NRL-CQD ones but similar to the

RL-CQDs-5 and NL-CQDs-3 ones. Therefore, the intense NRL-CQD fluorescence was not simply due to physical mixing but due to the amino and hydroxyl groups chemically introduced to the L-CQD surface, thus intensifying the fluorescence considerably. Figure 4 (c) shows an optical photograph of L-CQDs-3, RL-CQDs-5, NL-CQDs-3, and NRL-CQDs irradiated with a 365-nm UV light. As shown, introducing both electron-donating substituents significantly intensifies the L-CQDs-3 fluorescence while synergistically maximizing the NRL-CQD fluorescence intensity.

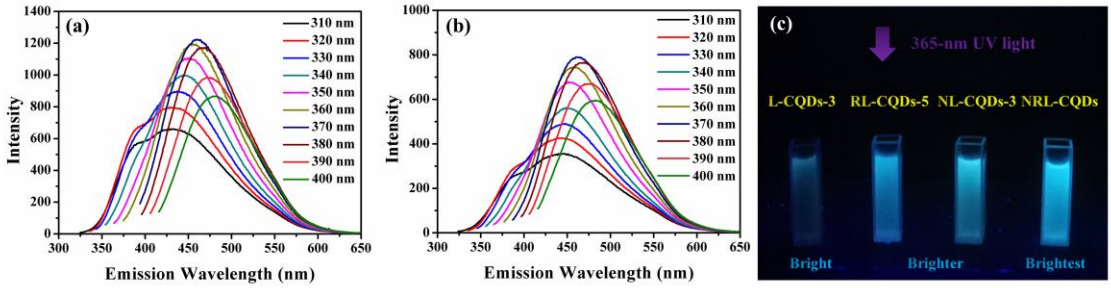

Figure 4. (a) PL spectra generated for NRL-CQDs and (b) NL-CQDs-3 mixed with RL-CQDs-5 with the excitation wavelength from 310 nm to 400 nm, and (c) optical photographs of L-CQDs-3, RL-CQDs-5, NL-CQDs-3, and NRL-CQDs irradiated using 365-nm UV light.

L-CQD chemical properties

FT-IR spectroscopy was first used to characterize the chemical structures of the L-CQD samples, as shown in Figure S3. The positions of the absorption peaks of the CQDs were very similar, indicating that both modifications might only change the number, not the type, of L-CQD functional groups. The L-CQDs mainly exhibited C-C and C=C bonds and some oxygen-containing functional groups such as -OH, C=O, and C-O and some nitrogen-containing ones such as C=N, C-N, and N-H. The L-CQD-

specific peak positions and types are listed in Table S1.

XPS was used to analyze the L-CQDs, RL-CQDs-5, and NL-CQDs-3 surface compositions and the content and types of functional groups. The XPS full-spectrum scan is shown in Figure 5 (a). The L-CQDs were mainly composed of C (73.02%) and O (25.31%) and a very small amount of N (1.67%). The N might have originated from the protein in the plant material. The C, O, and N narrow-spectrum scans were then collected, and the obtained peak areas were integrated using XPSPEAK 4.1 software. As shown in Figure 5 (b), the high-resolution L-CQD C 1*s* spectrum shows three main peaks at 283.4, 284.7, and 286.65 eV, corresponding to C=C/C-C/C-H (45.51%), C-O (39.77%), and C=O (14.72%) [31], respectively. Figure 5 (c) shows the high-resolution L-CQD N 1*s* spectra, and the peaks were deconvoluted using the method developed by Wu et al. [32]. The L-CQD N atoms were present as 11.54% graphitic, 22.06% pyrrolic, 39.04% amino, and 27.36% pyridinic N at 401.38, 399.99, 398.74, and 397.17 eV, respectively, among which the amino-N content was the highest, at approximately 0.34. Furthermore, the O 1*s* spectra in Figure 5 (d) exhibits peaks at 530.06, 531.31, and 532.46 eV corresponding to aromatic ether bonds and C=O (27.85%), C-O/C-O-C (47.49%), and -OH (24.66%) [28], respectively. The hydroxyl-group content was approximately 5.37%. The XPS results suggested that the L-CQDs might consist of a nitrogen-doped aromatic-polymer structure exhibiting a carbon–carbon-bond framework accompanied by numerous oxygen-containing functional groups (such as hydroxyl, carboxyl, carbonyl, aldehyde, or methoxy groups) and a few amino and heterocyclic groups.

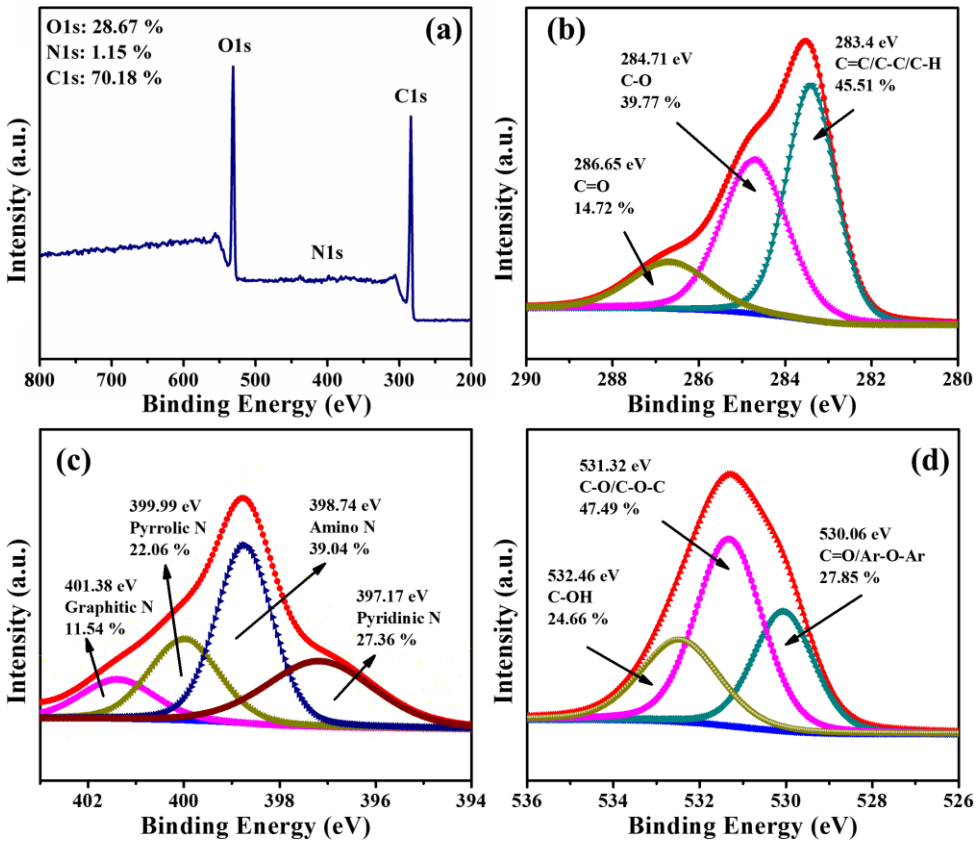

Figure 5. (a) XPS full-spectrum scan and (b) C 1*s*, (c) N 1*s*, and (d) O 1*s* high-resolution XPS fitting spectra generated for L-CQDs.

As shown in the RL-CQDs-5 full-spectrum scan in Figure S4 (a), the main RL-CQDs-5 elements were C, N, and O, accounting for 73.02, 1.67, and 25.31%, respectively, which were almost identical to the L-CQD element compositions. Furthermore, the changes in the RL-CQDs-5 functional-group contents were analyzed using XPS narrow-spectrum scanning. Together, the C 1*s* spectra in Figure S4 (b) and Figure S4 (b) clearly show that the RL-CQDs-5 bond types did not change and that the C–C and C–O bonds were still the main types. However, after the L-CQDs were reduced using $NaBH_4$, the C=O-group content on the RL-CQDs-5 surface decreased from 14.72 to 6.68%, and the C–O-bond content increased from 39.77 to 46.83%

because $NaBH_4$ had reduced the aldehyde groups to hydroxyl ones on the RL-CQDs-5 surface, while the C–C-bond content remained unchanged. Figure S4 (c) compares the RL-CQDs-5 and L-CQD N 1*s* spectra, wherein the pyrrolic- and graphitic-N contents both increased, while the amino- and pyridinic-N contents both decreased. Although the RL-CQDs-5 amino-group adsorption capacity was approximately 0.39 $mmol \cdot g^{-1}$, the detection error was high owing to the extremely low RL-CQDs-5 nitrogen content. Therefore, the N 1*s* spectra were only used as a reference. Therefore, the O 1*s* spectra shown in Figure S4 (d) were used to further analyze the changes in the hydroxyl-group content of the L-CQDs reduced using $NaBH_4$. The hydroxyl-group content increased from 24.66 in RL-CQDs-5 to 57.13% in L-CQDs, while the RL-CQDs-5 hydroxyl-group content increased considerably to 11.08 $mmol \cdot g^{-1}$. The results indicate that the electron-donating substituent hydroxyl groups were introduced to the RL-CQDs-5 surface by reducing aldehyde groups.

The NL-CQDs-3 XPS full-spectrum scan is shown in Figure S5 (a). Compared with L-CQDs, the EDA-modified NL-CQDs-3 contained no other heteroatoms, and the N content increased from 2.76 to 12.37%, while the C and O contents accounted for 66.39 and 21.24%, respectively. According to the C 1*s* and O 1*s* spectra shown in Figure S5 (b) and Figure S5 (d), respectively, the contents of nitrogen- and oxygen-containing functional groups in both NL-CQDs-3 and L-CQDs were approximately identical, and no additional functional groups were identified. The NL-CQDs-3 N 1*s* spectrum is shown in Figure S5 (c). As shown, the graphitic- and pyrrolic-N contents increased and the amino- and pyridinic -N contents decreased in NL-CQDs-3 compared with L-CQDs.

Moreover, the amino-N content decreased from 39.04% in L-CQDs to 19.88% in NL-CQDs-3, suggesting that using EDA to nitrogen-dope the hydrothermally prepared L-CQDs mainly increased the NL-CQDs-3 graphitic- and pyrrolic-N contents. However, owing to the significantly increased nitrogen content (6.46%) in NL-CQDs-3 (compared to 1.15% in L-CQDs), the amino-N adsorption capacity in NL-CQDs-3 still increased significantly to approximately 0.98 mmol/g.

According to the relationship between the intensified fluorescence and the number of electron-donating substituents, for every 1 mmol of hydroxyl and amino groups in L-CQDs, the L-CQD fluorescence intensifies by 88.54 and 658.95, respectively. Clearly, the amino groups intensify the L-CQD fluorescence more strongly. However, introducing amino acids is usually limited by the type of amination reagent, and different amination reagents are usually more suitable for different raw materials. Moreover, introducing amino groups is more complex than introducing hydroxyl groups, which only requires reaction with sodium borohydride at room temperature.

Therefore, to determine whether combining amination and hydroxylation synergistically or antagonistically affects L-CQD fluorescence, XPS was used to quantitatively analyze the content of different NRL-CQD functional groups. Figure S6 (a) shows the NRL-CQD XPS full-spectrum scan exhibiting C, O, and N contents of 69.50, 24.90, and 5.60%, respectively. As shown in the C 1*s* spectrum in Figure S6 (b), compared with the C=O content in NL-CQDs-3 (13.42%) in Figure S6 (b), that was slightly decreased in NRL-CQDs (10.05%). This shows that part of C=O was reduced to -OH. The O 1*s* spectrum in Figure S6 (d) clearly shows that, compared to the C-OH

content (57.13%) in RL-CQDs-5, that was slightly lower (52.18%) in NRL-CQDs. The hydroxyl adsorption capacity of NRL-CQDs was 9.91 $mmol \cdot g^{-1}$, which was slightly lower than RL-CQDs-5 (11.08 $mmol \cdot g^{-1}$). These findings of O 1*s* spectrum indicate that after amination, some of the oxygen-containing functional groups in L-CQDs were replaced by amino-containing ones (the O/C ratio of NL-CQDs-3 was 36.12%, which was lower than 40.85% of L-CQDs). This result decreased the content of hydroxyl groups in NRL-CQDs upon reduction by $NaBH_4$, thus implying that amination should be antagonistic to hydroxylation. The N 1*s* spectrum in Figure S6 (c) clearly shows that compared with the amino-group content (19.88%) in NL-CQDs-3, that (26.48%) in NRL-CQDs was increased. This was because the $NaBH_4$ further reduced some NL-CQDs-3 nitrogen oxides (such as nitro groups). Although the NRL-CQD and NL-CQDs-3 N 1*s* spectra exhibit similar overall trends, the graphitic-N content decreased, which could be because some individual L-CQDs were cleaved by excess $NaBH_4$. The results led to exposing the internal graphitic-N groups and forming pyridinic- or pyrrolic-N ones in addition to being reduced by excess $NaBH_4$. Moreover, the amino-group adsorption capacity (1.13 mmol/g) of NRL-CQDs was slightly higher than that of NL-CQDs-3 (0.98 $mmol \cdot g^{-1}$). Therefore, the hydroxyl-group reduction was synergistic for amination. These results together with the optical-property analysis suggested that compared with the introduction of a single electron-donating substituent, the co-introduction of both amino and hydroxyl groups intensified the L-CQD fluorescence to a larger degree. Moreover, because the amino groups intensified the CQD fluorescence more than the hydroxyl groups did, lignin-based CQD fluorescence

was primarily intensified by hydroxyl-group-reduction-assisted amination.

L-CQD physical properties

TEM and AFM were used to analyze the CQD particle size and micromorphology, as shown in Figure 6. Figure 6 (a-d) clearly show spherical L-CQD particles well dispersed in water, which might be related to the combined effects of the L-CQD hydrophilic (hydroxyl, carboxyl, amino, etc.) and hydrophobic (alkyl, phenyl, etc.) groups [33]. The inset in Figure 6 (a) shows the L-CQD particle-surface topography observed by high-resolution TEM. The L-CQD surface exhibited a lattice fringe of 0.21 nm, corresponding to the (100)-diffraction plane of crystalline graphene and indicating the lamellar structure of L-CQDs [34]. Meanwhile, the carbon element content in L-CQDs (Figure 5. (a)) was up to 70.18%, so we believed that L-CQDs have a "lamellar graphene-like structure", which played the role of "core". The inset in Figure 6 (b) shows the average particle-size distribution obtained by randomly measuring the diameter of 100 particles with Nano Measurer software. The L-CQD particle-size distribution was in the range 3–10 nm, with an average size of 6.25 nm, which satisfied the traditional criterion for the CQD particle-size-distribution range (i.e., <10 nm) [35]. Based on these data, each independent L-CQD should be composed of 14 (3/0.21=14.29)—48 (10/0.21=47.62) layers of graphene-like sheets by calculation. Figure 6 (e) and (f-h) show the 3D and 2D L-CQD AFM images, respectively. AFM results show that L-CQDs were spherical and well dispersed, and the size distribution was nonuniform, which was consistent with the TEM results. The results of XPS also indicate that there were a large number of oxygen-containing functional groups such as

hydroxyl, methoxy and carbonyl on the surface of L-CQDs. Moreover, since L-CQDs had a complete graphene lattice inside observed by TEM, these oxygen-containing defective structures should only existed at the edge of graphene layers. Under the action of stacking, these oxygen-containing functional groups located on the edge of L-CQDs were accumulated to form the "oxygen-containing functional group shells" and wrap the internal lamellar graphene-like structure ("core"). Based on the above analysis, we believe that L-CQDs is a "core-shell lamellar structure" and consisted of 14–48 graphene-like sheets stacked together, with a lamellar graphene-like structure as the core and a large number of oxygen-containing functional groups on the outside as the shell, as shown in Scheme 1.

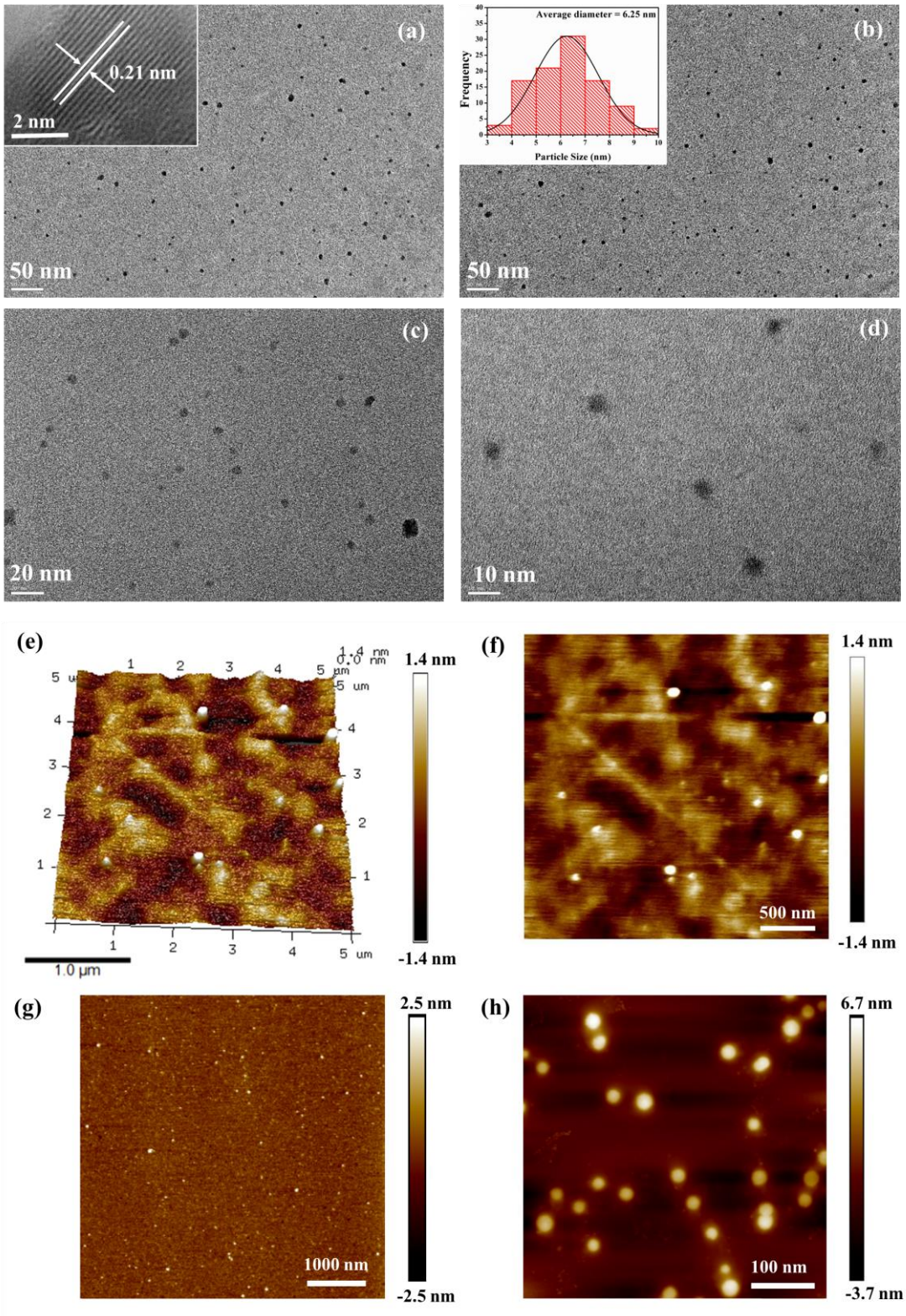

Figure 6. (a, b, c, d) TEM images of L-CQDs at different magnifications. Inserts in (a) and (b) show high-resolution L-CQD topography and particle-size distribution, respectively, and (e) 3D and (f, g, h) 2D L-CQD AFM images at different

magnifications.

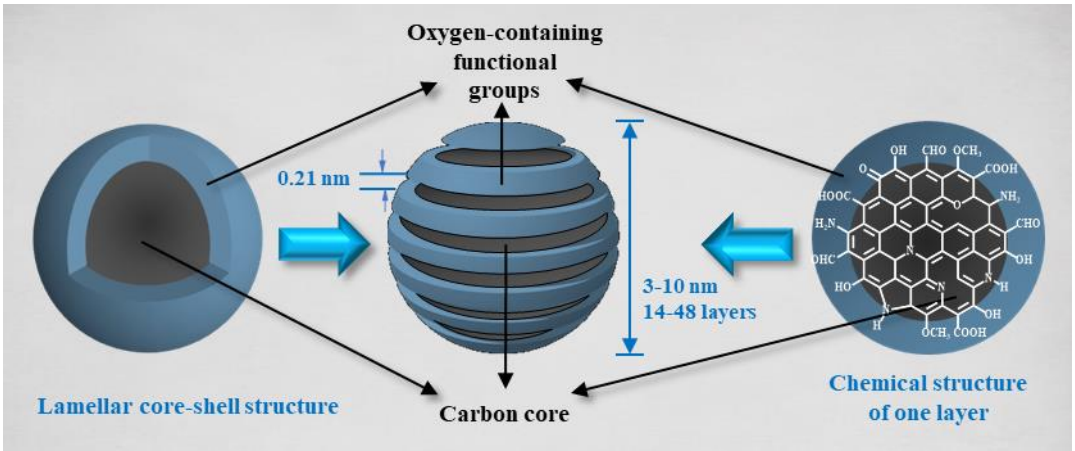

Scheme 1. L-CQD lamellar core–shell and chemical structures based on TEM, AFM and XPS analysis.

As shown in Figure S7, the changes in the micromorphology and particle size of RL-CQDs-5, NL-CQDs-3, and NRL-CQDs were characterized using TEM. Figure S7 (a), (c), and (e) clearly show that all the modified L-CQDs exhibited less dispersion than the original pristine ones, which might be because the increased hydroxyl- and amino-group contents strengthened the hydrogen bonding between the L-CQD particles, causing them to partially aggregate. In addition, when the prepared freeze-dried CQDs were redissolved in water during conducting the TEM images, some particles could not quickly separate under external forces, leading to particle agglomeration. However, compared with the traditional aggregation induced emission / quenching (AIE/AIQ) CQDs aggregate (more than 50 nm) [36], the aggregation phenomena (about 10 nm) of RL-CQDs-5 and NL-CQDs-3 was not serious, and independently dispersed CQDs were still clearly visible. Moreover, compared with that of L-CQDs, the fluorescence intensity of RL-CQDs and NL-CQDs solution increased several times after the

introduction of amino and hydroxyl groups on the surface of L-CQDs, as shown in Figure 2 (a) and Figure 3 (f). Therefore, even if a small amount of aggregation will affect the fluorescence effect of CQDs, these two modification methods also play an absolute role in promoting the fluorescence intensity of L-CQDs.

Introducing electron-donating substituents did not change the microscopic L-CQD morphology; that is, most RL-CQDs-5, NL-CQDs-3, and NRL-CQD particles remained regularly spherical, and the particle surfaces retained their initial lattice fringes, indicating that introducing the electron-donor groups to the particle surface did not destroy the L-CQD graphite structure. However, as shown in Figure S7 (b), the RL-CQDs-5 particle-size distribution revealed that the average RL-CQDs-5 particle size (2.42 nm) was considerably smaller than that of the original L-CQDs (6.25 nm). These results suggested $NaBH_4$, in addition to reducing L-CQDs, may cleave the L-CQD macromolecules resulting in smaller particle size. As shown in Figure S7 (d), the average NL-CQDs-3 particle size was 6.48 nm, which was very similar to that of L-CQD and suggested that amination did not change the basic L-CQD size. However, as shown in Figure S7 (f), similar to the RL-CQDs-5 particle size, the NRL-CQD size was also reduced to 3.53 nm, indicating that during NRL-CQD preparation, as NL-CQDs-3 was treated with increasing $NaBH_4$ concentrations, the $NaBH_4$ also cleaved the NL-CQDs-3, thereby confirming that the speculative NRL-CQD chemical structure determined using XPS analysis was correct. Together with the NL-CQDs-3 and NRL-CQD N 1*s* spectra shown in Figure S5 (c) and Figure S6 (d), respectively, this speculative "molecular cleaving" mechanism explains the decrease in NRL-CQD

graphitic-N content. Cleavage of the NL-CQDs-3 molecules exposes their internal graphitic-N groups; thus, more NRL-CQD pyridinic- and pyrrolic-N groups were formed. These results together with the quantum size effect [37] suggested that the intensified RL-CQDs-5 and NRL-CQD fluorescence may also be attributed to the formation of smaller particles. The quantum size effect asserts that the optimal CQD excitation and emission wavelengths both undergo a blueshift with decreasing CQD particle size [37]. However, according to the data presented in Table 1, the excitation and emission wavelengths of both RL-CQDs-X and NRL-CQDs were not blueshifted compared with those of L-CQDs (370 nm). Therefore, the RL-CQDs-X and NRL-CQD quantum size effects were not the main reason for the intensified L-CQD fluorescence.

L-CQD biocompatibility and application in cell imaging

With HepG2 cells as the object, the cytotoxicity of L-CQDs and NRL-CQDs was tested using the CCK-8 method [21]. Different volumes of L-CQDs and NRL-CQDs solutions (0.1 $mg \cdot mL^{-1}$) were added to the culture medium to test the biocompatibility of different concentrations of CQDs. The results are shown in Figure 7 (a) and (b). With the increase of the addition amount of L-CQDs and NRL-CQDs, the cell activity of HepG2 cells gradually decreased. When the volume of CQDs and culture medium were 1:5, the cell activity was still higher than 90% after 24 hours of incubation, and the compatibility of L-CQDs was slightly better than that of NRL-CQDs. Even if the volume ratio of CQDs to culture medium reached 1:1, more than 70% of the cells still survived. The above results indicate that both L-CQDs and modified NRL-CQDs had higher biocompatibility and lower cytotoxicity, and both had good application prospects

in the field of cell imaging.

The L-CQDs solution and NRL-CQDs solution (0.1 mg·mL^{-1}) were respectively incubated with HepG2 cells at 37° C for 24 h, and the incubated cells were observed under a fluorescence microscope (λ=395 nm), the volume ratio of CQDs solution to culture medium was 1:5. As shown in Figures 7 (c) and (d), the HepG2 cells cultured by L-CQDs could only emit weak blue fluorescence, and it was difficult to distinguish from the black background. However, when the cells were cultivated with fluorescence-enhanced NRL-CQDs, as shown in Figures 7 (e) and (f), the NRL-CQDs successfully entered the cells, and the fluorescence intensity of the cells in the field of view was significantly enhanced. The cells were more clearly distinguished from the background, and the positions of the cells corresponded to the bright field. In addition, the position of the cytoplasm and the nucleus could be clearly distinguished in the image. The cytoplasm was bright blue, while the nucleus was black. This shows that NRL-CQDs mainly existed in the cytoplasm and basically did not enter the nucleus. This might be because that the permeability of the nuclear membrane is lower than that of the cell membrane, thus CQDs cannot enter the nucleus by simple free diffusion or active transport, which is consistent with previous reports [38]. The above results indicate that the introduction of electron-donating substituents has led to more successful cell imaging. The fluorescence enhancement modification method in this study makes biomass-based CQDs with low quantum yields have greater potential in biological imaging.

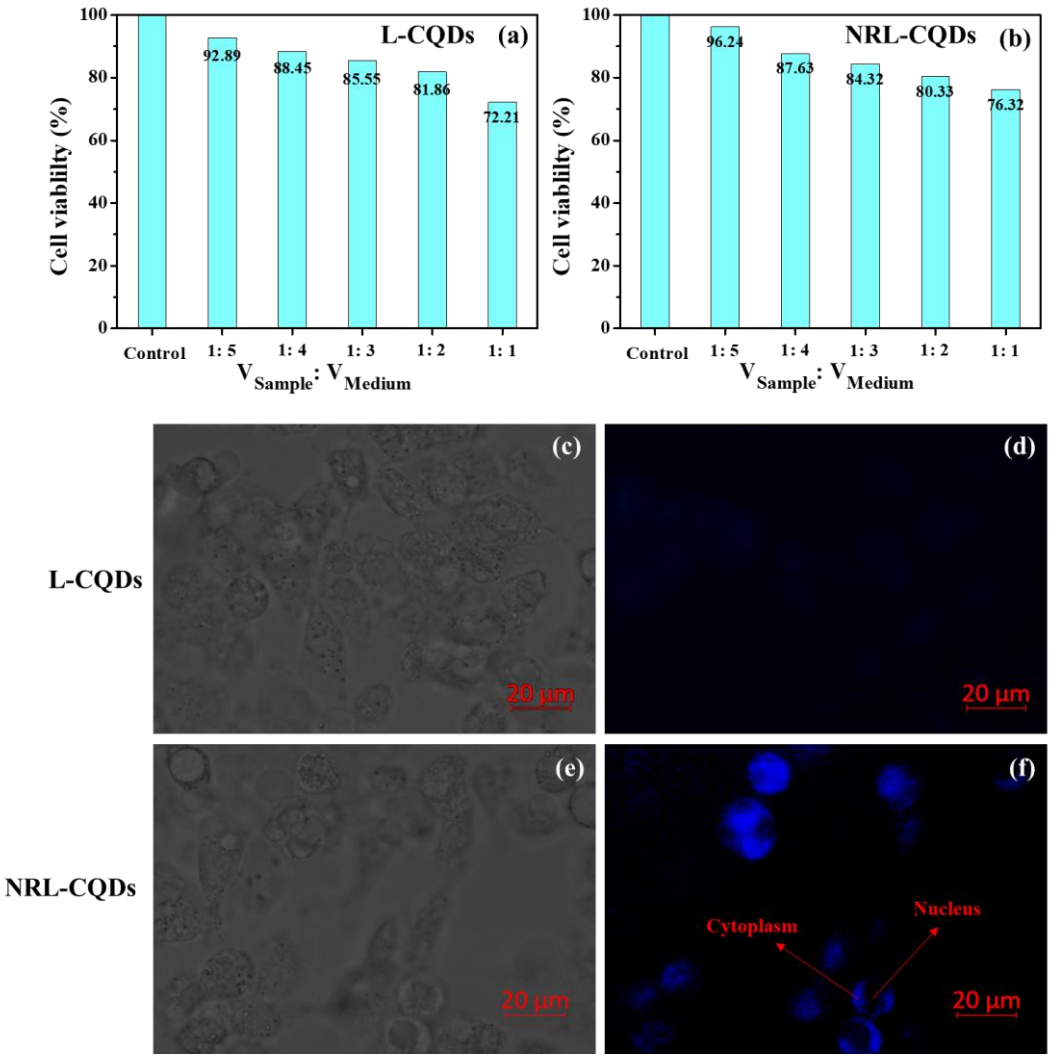

Figure 7. Cell viability values (%) evaluated by CCK-8 method after incubation with (a) L-CQDs and (b) NRL-CQDs under different concentrations at 37 °C for 24 h; Bright-field images (c, e) and fluorescence microscope images (λ=395 nm) (d, f) of HepG2 cells incubated with L-CQDs and NRL-CQDs for 12 h under 37 ℃, respectively.

CONCLUSION

Lignin extracted from bagasse-based caustic-soda black liquor was used as a raw material to hydrothermally prepare lignin-based carbon quantum dots (L-CQDs) using a one-pot method. Physicochemical characterization suggested that the L-CQDs

exhibited a lamellar core–shell structure consisting of a multilayered graphene carbon core wherein each layer was surrounded by oxygen-containing functional groups. To intensify the weak fluorescence of traditional hydrothermally prepared biomass-based L-CQDs, the optimal L-CQD concentration was first determined through L-CQD-concentration-dependent L-CQD fluorescence tests to maximize the L-CQD fluorescence and found to be most intense at an L-CQD concentration of 0.1 $mg \cdot mL^{-1}$. The L-CQD fluorescence was further intensified by introducing electron-donating substituents (i.e., hydroxyl and amino groups) to the L-CQD surface. When the L-CQD hydroxyl-group adsorption capacity increased from 5.37 to 11.08 $mmol \cdot g^{-1}$, the fluorescence intensified from 183.66 to 689.22. When the L-CQD amino-group adsorption capacity increased from 0.34 to 0.98 $mmol \cdot g^{-1}$, the fluorescence intensified from 183.66 to 605.39. However, when amination and hydroxylation were conducted sequentially to prepare L-CQDs exhibiting high-intensity fluorescence, the NRL-CQD fluorescence intensified to 1224.92. These results in combination with those of chemical analysis demonstrated that the introduction of both electron-donating substituents both synergistically and antagonistically intensified the L-CQD fluorescence. The L-CQD fluorescence was intensified by both methods, which is important for improving the usually poor fluorescence of hydrothermally prepared biomass-based CQDs. Cell imaging experiments also proved that the cells cultivated with NRL-CQDs had brighter fluorescence in the field of view than L-CQDs, and the cell outline was more obvious.

ASSOCIATED CONTENT

Supporting Information

Entire experimental procedure; PL spectra of RL-CQDs-2 and RL-CQDs-3; UV–vis and bandgap spectra of L-CQDs, RL-CQDs-5, and NL-CQDs-3; FT-IR spectra of L-CQDs, RL-CQDs-5, and NL-CQDs-3; XPS full-spectrum and C 1s, N 1s, O 1s fitting spectra of RL-CQDs-5, NL-CQDs-3 and NRL-CQDs; TEM images and particle-size distributions of RL-CQDs-5, NL-CQDs-3, and NRL-CQDs.

AUTHOR INFORMATION

Corresponding Author

Xueping Song — College of Light Industry and Food Engineering, Guangxi University, Nanning, 530004, PR China; Guangxi Key Laboratory of Clean Pulp & Papermaking and Pollution Control, Nanning, 530004, PR China. Email: sx_ping@gxu.edu.cn

Notes

The authors declare no competing financial interest.

ACKNOWLEDGMENTS

The project was sponsored by the National Natural Science Foundation of China (Grant Nos. 21766002), Natural Science Foundation of Guangxi Province, China (Grant Nos. 2021GXNSFDA196006) and the Foundation of Guangxi Key Laboratory of Clean Pulp & Papermaking and Pollution Control, College of Light Industry and Food Engineering, Guangxi University (Grant Nos. 2021KF20).

REFERENCES

(1) Zaied, M.; Bellakhal, N. Electrocoagulation Treatment of Black Liquor From Paper

Industry. *J. Hazard. Mater.* **2009**, *163* (2-3), 995-1000. DOI: 10.1016/j.jhazmat.2008.07.115.
(2) Zevallos Torres, L. A.; Lorenci Woiciechowski, A.; de Andrade Tanobe, V. O.; Karp, S. G.; Guimarães Lorenci, L. C.; Faulds, C.; Soccol, C. R. Lignin as a Potential Source of High-added Value Compounds: A Review. *J. Clean Prod.* **2020**, *263*, 121499. DOI: 10.1016/j.jclepro.2020.121499.
(3) Gillet, S.; Aguedo, M.; Petitjean, L.; Morais, A. R. C.; da Costa Lopes, A. M.; Łukasik, R. M.; Anastas, P. T. Lignin Transformations for High Value Applications: Towards Targeted Modifications Using Green Chemistry. *Green Chem.* **2017**, *19* (18), 4200-4233. DOI: 10.1039/c7gc01479a.
(4) Xu, X.; Ray, R.; Gu, Y.; Ploehn, H. J.; Gearheart, L. A.; Raker, K.; Scrivens, W. A. Electrophoretic Analysis and Purification of Fluorescent Single-Walled Carbon Nanotube Fragments. *J. Am. Chem. Soc.* **2004**, *126* (40), 12736-12737.
(5) Zhao, P.; Zhu, L. Dispersibility of Carbon dots in Aqueous and/or Arganic Solvents. *Chem. Commun.* **2018**, *54* (43), 5401-5406. DOI: 10.1039/c8cc02279h.
(6) Han, M.; Zhu, S.; Lu, S.; Song, Y.; Feng, T.; Tao, S.; Liu, J.; Yang, B. Recent Progress on the Photocatalysis of Carbon Dots: Classification, Mechanism and Applications. *Nano Today* **2018**, *19*, 201-218. DOI: 10.1016/j.nantod.2018.02.008.
(7) Rong, M.; Feng, Y.; Wang, Y.; Chen, X. One-pot Solid Phase Pyrolysis Synthesis of Nitrogen-doped Carbon Dots for Fe^{3+} Sensing and Bioimaging. *Sens. Actuator B-Chem.* **2017**, *245*, 868-874. DOI: 10.1016/j.snb.2017.02.014.
(8) Li, D.; Jing, P.; Sun, L.; An, Y.; Shan, X.; Lu, X.; Zhou, D.; Han, D.; Shen, D.; Zhai, Y.; et al. Near-Infrared Excitation/Emission and Multiphoton-Induced Fluorescence of Carbon Dots. *Adv. Mater.* **2018**, *30* (13), e1705913. DOI: 10.1002/adma.201705913.
(9) Yang, G.; Wan, X.; Su, Y.; Zeng, X.; Tang, J. Acidophilic S-doped Carbon Quantum Dots Derived from Cellulose Fibers and Their Fluorescence Sensing Performance for Metal Ions in an Extremely Strong Acid Environment. *J. Mater. Chem. A* **2016**, *4* (33), 12841-12849. DOI: 10.1039/c6ta05943k. Yang, P.; Zhu, Z.; Chen, M.; Chen, W.; Zhou, X. Microwave-assisted Synthesis of Xylan-derived Carbon Quantum Dots for Tetracycline Sensing. *Opt. Mater.* **2018**, *85*, 329-336. DOI: 10.1016/j.optmat.2018.06.034.
(10) Achilleos, D.; Yang, W.; Kasap, H.; Savateev, A.; Reisner, E. Solar Reforming of Biomass with Homogeneous Carbon Dots. *Angew. Chem.-Int. Edit.* **2020**, *59* (47), 18184-18188. DOI: 10.1002/anie.202008217.
(11) Duan, Q.; Ma, L.; Zhang, B.; Zhang, Y.; Li, X.; Wang, T.; Zhang, W.; Li, Y.; Sang, S. Construction and Application of Targeted Drug Delivery System Based on Hyaluronic Acid and Heparin Functionalised Carbon Dots. *Colloid Surf. B-Biointerfaces* **2020**, *188*, 110768. DOI: 10.1016/j.colsurfb.2019.110768.
(12) Zhao, S.; Song, X.; Chai, X.; Zhao, P.; He, H.; Liu, Z. Green Production of Fluorescent Carbon Quantum Dots Based on Pine Wood and its Application in the Detection of Fe^{3+}. *J. Clean Prod.* **2020**, *263*, 121561. DOI: 10.1016/j.jclepro.2020.121561.
(13) Huang, Q.; Li, Q.; Chen, Y.; Tong, L.; Lin, X.; Zhu, J.; Tong, Q. High Quantum Yield Nitrogen-doped Carbon Dots: Green Synthesis and Application as “Off-On”

Fluorescent Sensors for the Determination of Fe^{3+} and Adenosine Triphosphate in Biological Samples. *Sens. Actuator B-Chem.* **2018**, *276*, 82-88. DOI: 10.1016/j.snb.2018.08.089.
(14) Lv, P.; Yao, Y.; Li, D.; Zhou, H.; Naeem, M. A.; Feng, Q.; Huang, J.; Cai, Y.; Wei, Q. Self-assembly of Nitrogen-doped Carbon Dots Anchored on Bacterial Cellulose and Their Application in Iron Ion Detection. *Carbohydr. Polym.* **2017**, *172*, 93-101. DOI: 10.1016/j.carbpol.2017.04.086.
(15) Li, W.; Zhang, Z.; Kong, B.; Feng, S.; Wang, J.; Wang, L.; Yang, J.; Zhang, F.; Wu, P.; Zhao, D. Simple and Green Synthesis of Nitrogen-doped Photoluminescent Carbonaceous Nanospheres for Bioimaging. *Angew. Chem.-Int. Edit.* **2013**, *52* (31), 8151-8155. DOI: 10.1002/anie.201303927.
(16) Williams, R. T.; Bridges, J. W. Fluorescence of Solutions: A review. *J. Clin. Pathol.* **1964**, *17*, 371-394. DOI: 10.1136/jcp.17.4.371.
(17) Xu, J.; Wang, Z. *Fluorescence Analysis*; Science Press, 2006.
(18) Ju, J.; Chen, W. Synthesis of Highly Fluorescent Nitrogen-doped Graphene Quantum Dots for Sensitive, Label-free Detection of Fe (III) in Aqueous Media. *Biosens. Bioelectron.* **2014**, *58*, 219-225. DOI: 10.1016/j.bios.2014.02.061.
(19) Shen, D.; Long, Y.; Wang, J.; Yu, Y.; Pi, J.; Yang, L.; Zheng, H. Tuning the Fluorescence Performance of Carbon Dots with a Reduction Pathway. *Nanoscale* **2019**, *11* (13), 5998-6003. DOI: 10.1039/c8nr09587f.
(20) Liu, Z.; Chen, M.; Guo, Y.; Zhou, J.; Shi, Q.; Sun, R. Oxidized Nanocellulose Facilitates Preparing Photoluminescent Nitrogen-doped Fluorescent Carbon Dots for Fe^{3+} Ions Detection and Bioimaging. *Chem. Eng. J.* **2020**, *384*, 123260. DOI: 10.1016/j.cej.2019.123260.
(21) Jeong, Y.; Moon, K.; Jeong, S.; Koh, W.; Lee, K. Converting Waste Papers to Fluorescent Carbon Dots in the Recycling Process without Loss of Ionic Liquids and Bioimaging Applications. *ACS Sustain. Chem. Eng.* **2018**, *6* (4), 4510-4515. DOI: 10.1021/acssuschemeng.8b00353.
(22) Zhang, Y.; Zhuo, P.; Yin, H.; Fan, Y.; Zhang, J.; Liu, X.; Chen, Z. Solid-State Fluorescent Carbon Dots with Aggregation-Induced Yellow Emission for White-Light-Emitting Diodes with High Luminous Efficiencies. *ACS Appl. Mater. Interfaces* **2019**, *11* (27), 24395-24403. DOI: 10.1021/acsami.9b04600.
(23) Shao, J.; Zhu, S.; Liu, H.; Song, Y.; Tao, S.; Yang, B. Full-Color Emission Polymer Carbon Dots with Quench-Resistant Solid-State Fluorescence. *Adv. Sci.* **2017**, *4* (12), 1700395. DOI: 10.1002/advs.201700395.
(24) Wang, C.; Hu, T.; Wen, Z.; Zhou, J.; Wang, X.; Wu, Q.; Wang, C. Concentration-dependent Color Tunability of Nitrogen-doped Carbon Dots and Their Application for Iron(III) Detection and Multicolor Bioimaging. *J. Colloid Interface Sci.* **2018**, *521*, 33-41. DOI: 10.1016/j.jcis.2018.03.021.
(25) Ba, X. X.; Zhang, L.; Yin, Y. L.; Jiang, F. L.; Jiang, P.; Liu, Y. Luminescent Carbon Dots with Concentration-dependent Emission in Solution and Yellow Emission in Solid State. *J. Colloid Interface Sci.* **2020**, *565*, 77-85. DOI: 10.1016/j.jcis.2020.01.007.
(26) Cushing, S. K.; Li, M.; Huang, F.; Wu, N. Origin of Strong Excitation Wavelength Dependent Fluorescence of Graphene Oxide. *ACS Nano* **2014**, *8* (1), 1002-1013.

(27) Haase, M.; Schäfer, H. Upconverting Nanoparticles. *Angew. Chem.-Int. Edit.* **2011**, *50* (26), 5808-5829. DOI: 10.1002/anie.201005159.
(28) Si, M.; Zhang, J.; He, Y.; Yang, Z.; Yan, X.; Liu, M.; Zhuo, S.; Wang, S.; Min, X.; Gao, C.; et al. Synchronous and Rapid Preparation of Lignin Nanoparticles and Carbon Quantum Dots from Natural Lignocellulose. *Green Chem.* **2018**, *20* (15), 3414-3419. DOI: 10.1039/c8gc00744f.
(29) Chai, X.; He, H.; Fan, H.; Kang, X.; Song, X. A Hydrothermal-carbonization Process for Simultaneously Production of Sugars, Graphene Quantum Dots, and Porous Carbon from Sugarcane Bagasse. *Bioresour. Technol.* **2019**, *282*, 142-147. DOI: 10.1016/j.biortech.2019.02.126.
(30) Chen, Y. Q.; Lian, H. Z.; Wei, Y.; He, X.; Chen, Y.; Wang, B.; Zeng, Q. G.; Lin, J. Concentration Induced Multi-color Emission in Carbon Dots: Origination From Triple Fluorescent Centers. *Nanoscale* **2018**, *10* (14), 6734-6743. DOI: 10.1039/c8nr00204e.
(31) Liu, Y.; Yang, H.; Ma, C.; Luo, S.; Xu, M.; Wu, Z.; Li, W.; Liu, S. Luminescent Transparent Wood Based on Lignin-Derived Carbon Dots as a Building Material for Dual-Channel, Real-Time, and Visual Detection of Formaldehyde Gas. *ACS Appl. Mater. Interfaces* **2020**, *12* (32), 36628-36638. DOI: 10.1021/acsami.0c10240.
(32) Wu, Q.; Li, W.; Tan, J.; Wu, Y.; Liu, S. Hydrothermal Carbonization of Carboxymethylcellulose: One-pot Preparation of Conductive Carbon Microspheres and Water-soluble Fluorescent Carbon Nanodots. *Chem. Eng. J.* **2015**, *266*, 112-120. DOI: 10.1016/j.cej.2014.12.089.
(33) Zhu, Z.; Yang, P.; Chen, M.; Zhang, T.; Cao, Y.; Zhang, W.; Zhou, X.; Chen, W. Microwave Synthesis of Amphiphilic Carbon Dots from Xylose and Construction of Luminescent Composites with Shape Recovery Performance. *J. Lumines.* **2019**, *213*, 474-481. DOI: 10.1016/j.jlumin.2019.05.006.
(34) Wang, R.; Xia, G.; Zhong, W.; Chen, L.; Chen, L.; Wang, Y.; Min, Y.; Li, K. Direct Transformation of Lignin into Fluorescence-switchable Graphene Quantum Dots and Their Application in Ultrasensitive Profiling of a Physiological Oxidant. *Green Chem.* **2019**, *21* (12), 3343-3352. DOI: 10.1039/c9gc01012b. Wang, Z.; Yuan, F.; Li, X.; Li, Y.; Zhong, H.; Fan, L.; Yang, S. 53% Efficient Red Emissive Carbon Quantum Dots for High Color Rendering and Stable Warm White-Light- Emitting Diodes. *Adv. Mater.* **2017**, *29* (37), 1702910. DOI: 10.1002/adma.201702910.
(35) Gao, X.; Du, C.; Zhuang, Z.; Chen, W. Carbon Quantum Dot-based Nanoprobes for Metal Ion Detection. *J. Mater. Chem. C* **2016**, *4* (29), 6927-6945. DOI: 10.1039/c6tc02055k. Molaei, M. J. A Review on Nanostructured Carbon Quantum Dots and Their Applications in Biotechnology, Sensors, and Chemiluminescence. *Talanta* **2019**, *196*, 456-478. DOI: 10.1016/j.talanta.2018.12.042.
(36) Nayak, S.; Das, P.; Singh, M. K. Carbon Dot with Aggregation Induced Emission and pH Triggered Disintegration. *Colloid Interface Sci. Commun.* **2021**, *45*, 100537. DOI: 10.1016/j.colcom.2021.100537.
(37) Kim, S.; Hwang, S. W.; Kim, M. K.; Shin, D. Y.; Shin, D. H.; Kim, C. O.; Yang, S. B.; Park, J. H.; Hwang, E.; Choi, S. H. Anomalous Behaviors of Visible Luminescence from GrapheneQuantum Dots: Interplay between Size and Shape. *ACS Nano* **2012**, *6* (9), 8203-8208.

(38) Xue, B.; Yang, Y.; Sun, Y.; Fan, J.; Li, X.; Zhang, Z. Photoluminescent Lignin Hybridized Carbon Quantum Dots Composites for Bioimaging Applications. *Int. J. Biol. Macromol.* **2019**, *122*, 954-961. DOI: 10.1016/j.ijbiomac.2018.11.018.

Table of content